## Electric-Field-Induced Coherent Control of Nitrogen-Vacancy Centers

Gerald Q. Yan, <sup>1</sup> Senlei Li, <sup>1</sup> Tatsuya Yamamoto<sup>®</sup>, <sup>2</sup> Mengqi Huang, <sup>1</sup> Nathan J. Mclaughlin, <sup>1</sup> Takayuki Nozaki<sup>®</sup>, <sup>2</sup> Hailong Wang, <sup>3</sup> Shinji Yuasa<sup>®</sup>, <sup>2</sup> and Chunhui Rita Du<sup>®</sup>, <sup>3</sup>, \*

<sup>1</sup>Department of Physics, University of California, San Diego, La Jolla, California 92093, USA
<sup>2</sup>National Institute of Advanced Industrial Science and Technology (AIST), Research Center for Emerging Computing Technologies, Tsukuba, Ibaraki 305-8568, Japan

<sup>&</sup>lt;sup>3</sup>Center for Memory and Recording Research, University of California, San Diego, La Jolla, California 92093-0401, USA



(Received 24 January 2022; revised 16 June 2022; accepted 14 November 2022; published 12 December 2022)

Enabling scalable and energy-efficient control of spin defects in solid-state media is desirable for realizing transformative quantum information technologies. Exploiting voltage-controlled magnetic anisotropy, we report the coherent manipulation of nitrogen-vacancy (N-V) centers by spatially confined magnetic stray fields produced by a proximate resonant magnetic tunnel junction (MTJ). Remarkably, the coherent coupling between N-V centers and the MTJ can be systematically controlled by a dc bias voltage, allowing for appreciable electrical tunability in the presented hybrid system. In comparison with current state-of-the-art techniques, the demonstrated N-V-based quantum operational platform exhibits significant advantages in scalability, device compatibility, and energy efficiency, further expanding the role of N-V centers in a broad range of quantum computing, sensing, and communications applications.

DOI: 10.1103/PhysRevApplied.18.064031

Over the past decade, nitrogen-vacancy (N-V) centers, which are optically active spin defects in diamond with single-spin addressability, excellent quantum coherence, and remarkable functionality over a broad range of temperatures, have emerged as a promising platform for developing transformative quantum information science and technology [1–3]. N-V centers have already been successfully applied to quantum sensing [2–4], imaging [5–8], communication [9–11], and network research [10–12], enabling high field sensitivity, nanoscale spatial resolution, and long-range qubit transmission. Hybrid systems establishing strong coupling between N-V centers, photons, and other solid-state media for applications in functional quantum devices are also currently being developed [13–31].

Despite significant progress in developing optical entanglement and optimizing spin-coherence times [9–12], problems related to scalability, qubit density, and local qubit control remain to be solved to fully realize the potential of N-V centers for developing alternative quantum processors [16,30,32–34]. In the current state of the art, the quantum spin state of N-V centers is typically manipulated by spatially dispersive Oersted fields generated by radio-frequency (rf) electric currents [35,36], imposing an inherent challenge for achieving highly local

and scalable manipulation of N-V centers. In addition, the current-induced Joule heating inherent to this approach can generate thermal noise, resulting in potential issues for developing N-V-based quantum processors consisting of multiple qubits in one diamond [37,38]. These long-standing issues have thus far hindered the development of N-V-based quantum computing platforms and proven profoundly difficult to overcome.

To address this challenge, we integrate N-V centers with a functional magnetic-tunnel-junction (MTJ) device exhibiting voltage-controlled magnetic anisotropy (VCMA) [39–41], enabling electric-field-driven coherent control of N-V centers in an energy-efficient manner. Manipulation of the spin qubits is achieved by exploiting the spatially confined magnetic stray fields produced by a resonant magnetic free layer within the MTJ stack. It is worth noting that the millisecond-long N-V spin-relaxation times ( $T_1$ ) are preserved in the presented hybrid system, offering an attractive platform for developing high-density scalable N-V-based solid-state architectures for applications at the forefront of quantum science and technologies.

We first describe the detailed structure of the device used in our measurements, as illustrated in Fig. 1(a). A MTJ composed of (from bottom to top) Ta(5 nm)/Co<sub>40</sub>Fe<sub>40</sub>B<sub>20</sub>(1 nm)/MgO(2 nm)/Co<sub>56</sub>Fe<sub>24</sub>B<sub>20</sub> (5 nm)/Ru(7 nm)/Cr(5 nm)/Au(50 nm) is fabricated on a Si substrate (see Appendix A for details). The in-plane magnetized Co<sub>56</sub>Fe<sub>24</sub>B<sub>20</sub> serves as a fixed reference layer,

<sup>\*</sup>c1du@physics.ucsd.edu

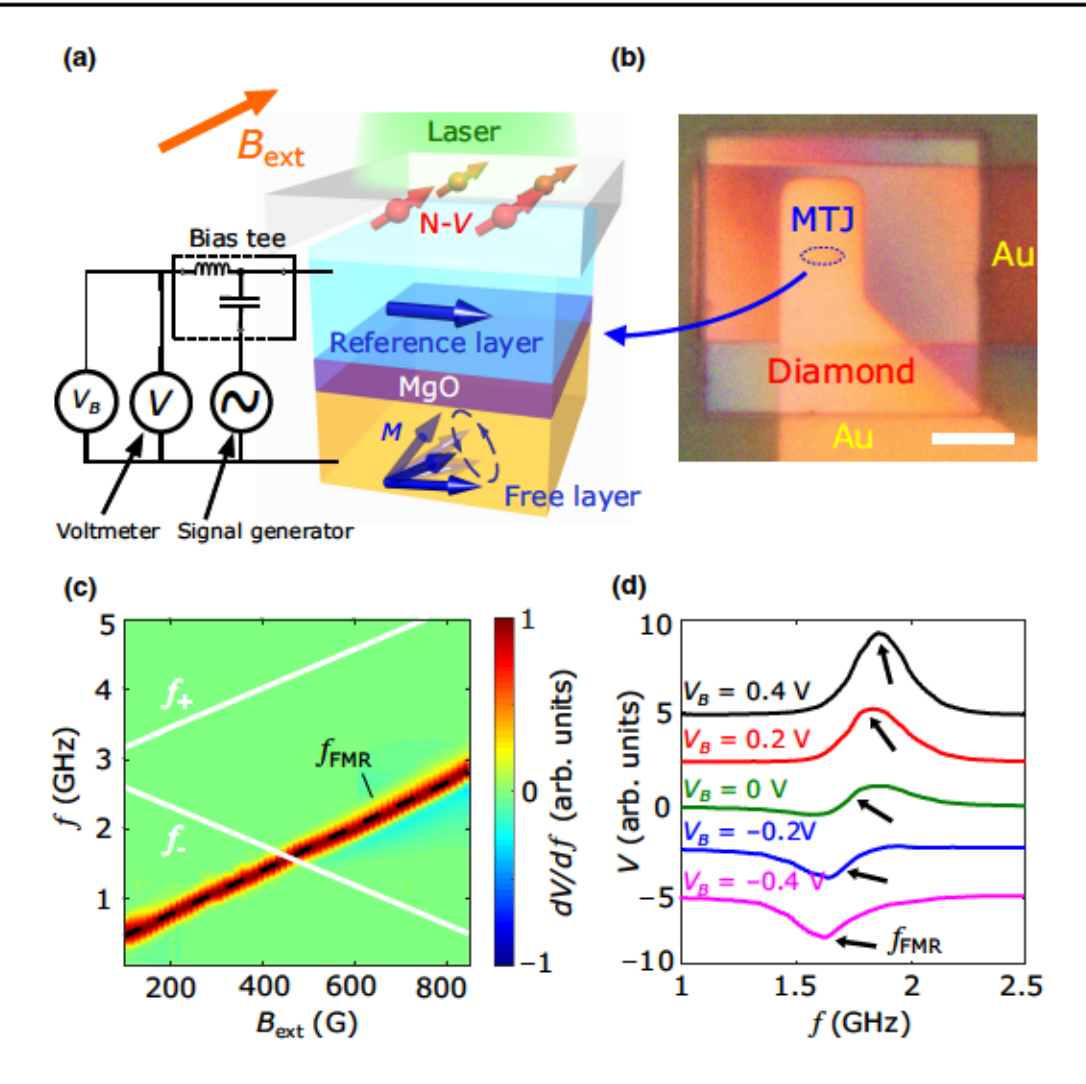


FIG. 1. (a) Schematic illustration of a N-V MTJ hybrid device. Diamond microchip containing N-V ensembles is placed on top of a prepared MTJ. N-V spin state is optically addressed using confocal or widefield microscopy. Electrical excitation and detection of VCMA-induced magnetic resonance utilizes a standard homodyne detection circuit. (b) Optical image showing the prepared N-V MTJ device. Blue dashed line outlines the edges of the MTJ, and the scale bar is 10  $\mu$ m. (c) Derivative of measured dc voltage, dV/df, as a function of external magnetic field,  $B_{\rm ext}$ , and frequency, f, of the applied voltage. White lines represent the field-dependent upper and lower N-V electron-spin-resonance frequencies, f. Black dashed line represents the fitting using a modified Kittel equation. (d) Dc-bias-voltage-induced variation of spectrum shape and shift of the resonant frequency, fFMR, of a MTJ device measured at  $B_{\rm ext}$  = 490 G.

while  $\text{Co}_{40}\text{Fe}_{40}\text{B}_{20}$  forms the free layer with spontaneous perpendicular magnetization due to a weak out-of-plane anisotropy [42–46]. Viewed from above, the MTJ has an elongated hexagonal shape with a length of 6  $\mu$ m and a width of 2  $\mu$ m. A diamond microchip [7] with lateral dimensions of  $30 \times 30~\mu\text{m}^2$  is placed on top of the MTJ. N-V centers are shallowly implanted on the bottom surface of the diamond chip with a density of about 1500 per  $\mu$ m<sup>2</sup>, and the distance between the N-V centers and the top surface of the MTJ stack is estimated to be about 200 nm. The optical image shown in Fig. 1(b) provides an overview of the prepared device. In our experiments, N-V centers are optically addressed using either confocal or widefield microscopy [6,47–49]. To enable

coherent control of the N-V centers, we take advantage of the oscillating magnetic stray fields generated by the proximate resonant MTJ. Applying a voltage across the MTJ modifies the electron charge or spin densities at the Co<sub>40</sub>Fe<sub>40</sub>B<sub>20</sub>/MgO interface and induces a variation of the magnetic anisotropy in the free layer through the spin-orbit interaction [41,50–53]. Due to the VCMA, the magnetic easy axis varies between the out-of-plane and in-plane directions, depending on the sign and magnitude of the applied voltage. Therefore, applying a rf voltage to the MTJ can excite coherent magnetic oscillations of the Co<sub>40</sub>Fe<sub>40</sub>B<sub>20</sub> free layer under an appropriate static external magnetic field, where the magnetic sample is driven under resonant conditions.

The experimental measurements of VCMA-driven ferromagnetic resonance (FMR) of the MTJ using a homodyne detection technique [39] are shown in Fig. 1(a). An external magnetic field,  $B_{\rm ext}$ , is applied at an angle of 54° relative to the out-of-plane direction, in alignment with the corresponding N-V axis. The in-plane projection of  $B_{\text{ext}}$ lies along the long axis of the MTJ, and a rf voltage with a power of -2 dBm is applied across the MTJ via the rf input port of a bias tee. Under FMR conditions, the oscillating tunnel magnetoresistance of the MTJ couples with the rf tunnel current to produce a significant dc voltage, V, which can be detected through the dc port of the bias tee. In this way, an output dc voltage is measured as a function of input frequency. Figure 1(c) plots a two-dimensional (2D) map of the derivative of the measured dc voltage with respect to frequency as a function of  $B_{\text{ext}}$  and frequency, f, of the applied rf voltage. VCMA-induced FMR is observed with expected field and frequency dependence, in accordance with theoretical predictions (see Appendix A for details). The FMR dispersion curve intersects with the N-V electron-spin-resonance (ESR) frequency at a field of  $B_{\text{ext}}$ = 447 G and frequency of f = 1.62 GHz. Under a fixed external magnetic field,  $B_{\text{ext}}$ = 490 G, the resonant frequency of the MTJ can be tuned with VCMA by varying the dc bias voltage across the device, as shown in Fig. 1(d).

Next, we utilize confocal microscopy (see Appendix B for details) to perform Rabi oscillation measurements of N-V centers located in an area of about  $1 \times 1 \mu m^2$  of the diamond that is directly above the MTJ, demonstrating electric-field-driven coherent control of N-V centers. Before discussing the experimental details, we first briefly review the pertinent physical properties of N-V centers. A N-V center consists of a substitutional nitrogen atom adjacent to a carbon-atom vacancy in one of the nearestneighboring sites of a diamond crystal lattice [1-3]. The negatively charged N-V state has an S=1 electron spin in the ground state and serves as a three-level system. When an oscillating magnetic field at the N-V ESR frequencies,  $f_{\pm}$ , is applied at the N-V site, the N-V occupation probabilities will periodically oscillate between two different spin levels. These are referred to as Rabi oscillations [1-3] and are illustrated in Fig. 2(a). Here,  $f_{\pm}$  denote the N-V ESR

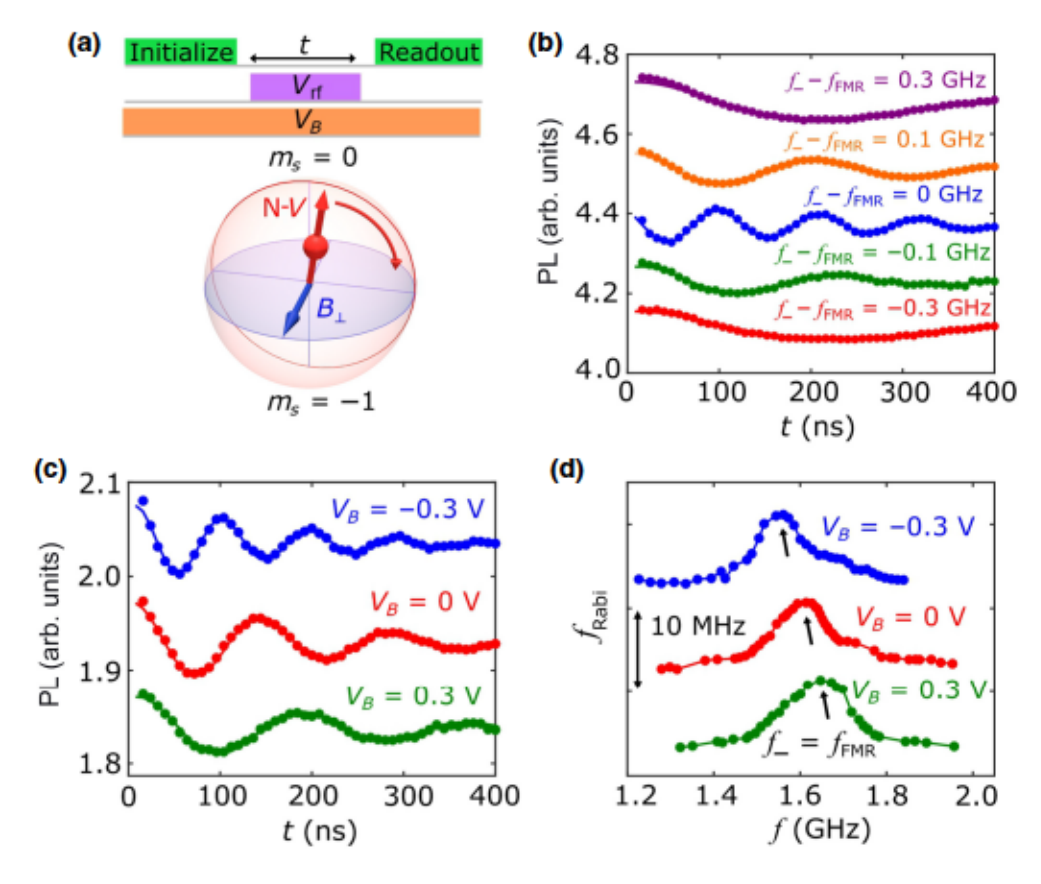


FIG. 2. (a) Top panel, optical and rf voltage pulse sequence used in the N-V Rabi oscillation measurements. Bottom panel, schematic of N-V Rabi oscillations between  $m_s = 0$  and  $m_s = -1$  states on the Bloch sphere. (b) N-V photoluminescence (PL) intensity as a function of delay time, t, measured at detuning frequencies ( $f_- - f_{\rm FMR}$ ) of  $\pm 0.3$ ,  $\pm 0.1$ , and 0 GHz. (c) Time-dependent N-V PL spectra measured with the application of dc bias voltages,  $V_B$ , of -0.3, 0, and 0.3 V under an external magnetic field,  $B_{\rm ext} = 470$  G. Rabi oscillation frequency is enhanced or suppressed, depending on the sign of the dc bias voltage. (d) Measured Rabi frequency as a function of N-V ESR frequency,  $f_-$ , under three different dc bias voltages. Curves are vertically offset for visual clarity.

frequencies corresponding to the spin transition between the  $m_s = 0$  and  $m_s = \pm 1$  states. Our N-V Rabi oscillation measurements are performed under N-V ESR conditions, and detuning is defined as the difference between the N-V ESR frequency and the resonant frequency,  $f_{FMR}$ , of the magnetic junction device. The top panel of Fig. 2(a) shows the specific measurement protocol. A 3- $\mu$ s-long greenlaser pulse is first applied to initialize the N-V centers to the  $m_s = 0$  state. Next, a rf voltage pulse at the N-V ESR frequencies is applied to excite the FMR of the MTJ. When the resonant frequency,  $f_{FMR}$ , matches  $f_{\pm}$ , oscillating stray fields generated by the MTJ will enhance the rate of the  $m_s = 0 \leftrightarrow \pm 1 \text{ N-V}$  spin transitions. Lastly, a second greenlaser pulse is applied to read out the N-V spin state via the spin-dependent photoluminescence (PL). The duration, t, of the rf voltage pulse is systematically varied to probe the time-dependent variation of the N-VPL. A dc bias voltage is also applied during the above measurements, providing electrical tunability of the coherent N-V-magnet coupling.

Figure 2(b) shows measured N-V Rabi oscillation spectra as a function of t at different N-V ESR frequencies. When  $f_{-}$  is detuned from the resonant frequency,  $f_{FMR}$ , of the MTJ such that  $|f_- - f_{FMR}| \ge 0.3$  GHz, the measured PL spectrum is essentially independent of the duration of the rf voltage pulse, indicating negligible N-V-magnet coupling. As f\_ approaches f<sub>FMR</sub>, the measured PL spectra exhibit characteristic periodic oscillations with a Rabi frequency,  $f_{Rabi}$ , of approximately 5 MHz at a detuning of  $\pm 0.1$  GHz. Remarkably, when  $f_{-} = f_{FMR}$ , we observe significantly faster oscillatory behavior of the N-V PL spectrum with an enhanced  $f_{Rabi}$  of about 10 MHz, demonstrating robust electric-field-induced coherent control of N-V spin states. The dramatic enhancement of the N-V spin-rotation rate is driven by phase synchronization between the resonant MTJ and proximate N-V centers. The Rabi oscillation frequency is proportional to the magnitude of the local magnetic stray field,  $B_{\perp}$ , transverse to the N-V spin orientation at the N-V site and is calculated to be 4.8 G, in agreement with theoretical calculations (see Appendix C for details). By applying a dc bias voltage,  $V_B$ , to vary the resonant frequency, f<sub>FMR</sub>, we are able to further achieve effective tuning of the N-V Rabi oscillation frequency through electric-field-induced variation of the static magnetic anisotropy [54,55], as shown in Fig. 2(c). Figure 2(d) plots the measured  $f_{Rabi}$  as a function of  $f_{-}$ for three different dc bias voltages.  $f_{FMR}$  shifts towards higher (lower) frequencies with positive (negative)  $V_B$ , due to a decrease (increase) of the perpendicular magnetic anisotropy. Peak values of  $f_{Rabi}$  are consistently observed when  $f_{-}$  matches  $f_{FMR}$ , demonstrating that the coherent N-V spin rotation is indeed driven by VCMA-induced FMR of the MTJ.

We next utilize widefield magnetometry (see Appendix B for details) to further illustrate the presented N-V control scheme and its electrical tunability. The laser-beam-spot

width used in the widefield measurements is approximately  $30 \times 30 \,\mu\text{m}^2$ , allowing simultaneous imaging of all the N-V centers in the diamond microchip that are positioned above the MTJ device. The N-V fluorescence is captured using a CMOS camera. Figures 3(a)-3(e) show a representative series of 2D widefield images of the measured N-V Rabi oscillation rate at five detuning frequencies  $(f_{-} - f_{FMR})$ , corresponding to points "A"—"E" shown in Fig. 3(f). At  $f_- = 1.49$  GHz [Fig. 3(a)], the measured N-V Rabi oscillation frequency,  $f_{Rabi}$ , is nearly negligible over the entire measured area due to a significant mismatch between the N-V ESR frequency and MTJ resonant frequency. Moderate N-V spin rotation emerges when  $f_{-} = 1.57$  GHz [Fig. 3(b)], suggesting the establishment of dipole-mediated coherent coupling between the resonant MTJ and N-V centers. The coupling strength is maximized when  $f_{-}$  matches  $f_{\rm FMR}$ , leading to the highest Rabi oscillation frequencies of the N-V centers directly above the MTJ [Fig. 3(c)]. Further increasing  $f_{-}$  results in detuning of the N-V center and VCMA FMR frequencies and subsequent suppression of the Rabi oscillation frequencies, as illustrated in Figs. 3(d) and 3(e). Note that the inhomogeneous distribution of the Rabi frequencies over the device indicates a spatially nonuniform distribution of the magnetic stray-field magnitudes produced by the MTJ, which can be tied to underlying magnetic inhomogeneities and domains in the device. Next, we consider the potential advantages of the presented N-V-based quantum operational platform. In contrast with conventional N-V-control schemes using spatially dispersive Oersted fields generated by rf currents, the N-V MTJ hybrid device utilizes magnetic stray fields, which are more spatially confined due to dipole-dipole interactions, to enable coherent control of N-V centers. To better illustrate this point, Fig. 3(g) shows one-dimensional profiles of the local magnetic stray field,  $B_{\perp}$  (transverse to the N-V axis), measured across the short axis of the MTJ at three N-V ESR frequencies. Notably,  $B_{\perp}$  shows a finite value at positions within the width of the MTJ device. At positions beyond the width of the device,  $B_{\perp}$  quickly decays to a vanishingly small value on a length scale of about 100 nm. Our experimental results agree with theoretical calculations (see Appendix D for details), confirming the highly localized N-V control strategy demonstrated by the presented N-V MTJ device. This merit is particularly beneficial for the development of high-density N-V-based information-processing and -storage technologies, where minimal crosstalk between neighboring operational units is desirable [19,56,57]. The solid-state nature of the MTJ devices and N-V centers renders them readily compatible with a large family of functional quantum architectures, promoting the use of N-V centers in implementing large-scale integrated quantum networks [11]. The voltage-controlled coherent N-V-magnet coupling is further illustrated in Figs. 4(a)-4(c). At  $B_{\text{ext}}$ = 460 G and  $f_{-} = 1.58$  GHz, application of a negative bias voltage of

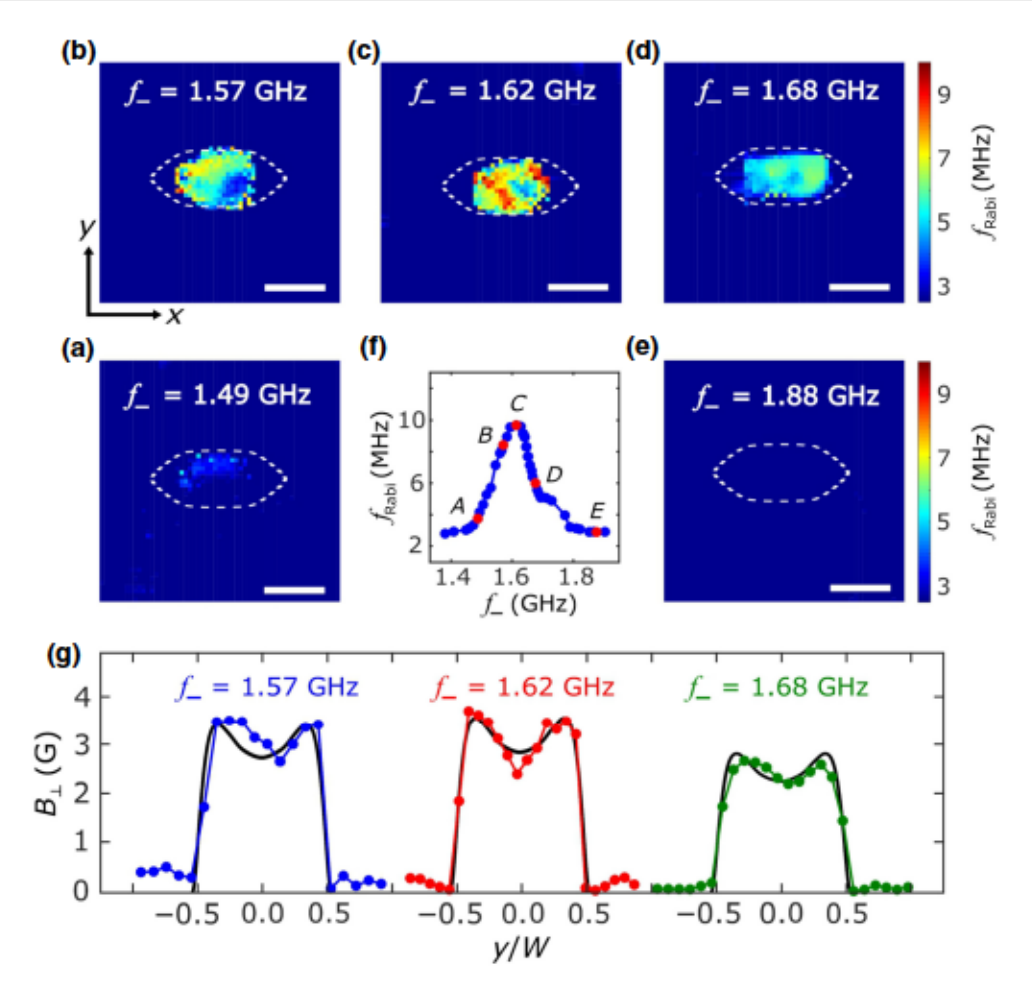


FIG. 3. (a)—(e) 2D maps of the Rabi oscillation frequency measured at N-V ESR frequencies,  $f_-$ , of 1.49, 1.57, 1.62, 1.68, and 1.88 GHz, respectively. White dashed line outlines the lateral boundary of the MTJ underneath the diamond chip, and the scale bar is 2  $\mu$ m. (f) Rabi oscillation frequency,  $f_{Rabi}$ , measured as a function of the ESR frequency,  $f_-$ , for N-V centers directly above the center of the MTJ. Points "A"—"E" marked on the curve correspond to the five N-V ESR frequencies,  $f_-$ , used in the N-V widefield magnetometry measurements presented in (a)—(e). (g) Line cuts of extracted magnetic stray field,  $B_\perp$  (transverse to the N-V axis), along the short axis (v axis) of the MTJ at ESR frequencies of 1.57, 1.62, and 1.68 GHz. Micromagnetic simulation results (black curves) are in qualitative agreement with experimental data. Unit of the v axis is normalized by the short-axis width (v = 2 v = 0 of the MTJ device.

-0.4 V significantly enhances the coherent N-V rotation rate [Fig. 4(a)], while a positive voltage effectively suppresses the N-V Rabi frequencies [Fig. 4(c)]. Our results demonstrate that the coherent N-V—magnet coupling can be electrically switched on and off by a moderate bias voltage. We expect that further optimization of the material and device parameters could add appreciable tunability of the N-V MTJ hybrid device across a broad range of experimental conditions.

Lastly, we perform N-V spin-relaxometry measurements using confocal microscopy to ascertain the spin-relaxation times  $(T_1)$  of the N-V centers directly above the MTJ. Our measurements are performed at  $B_{\rm ext}$ = 438 G and  $f_-$  = 1.64 GHz. At  $V_B$  = 0 V,  $f_-$  is close to  $f_{\rm FMR}$ , which is the minimum frequency of the magnon band. Application of a dc bias voltage shifts  $f_{\rm FMR}$  higher or lower

than  $f_{-}$ , depending on the sign of the voltage, as illustrated in Fig. 4(d). The top panel of Fig. 4(e) shows the optical and rf sequence used in the N-V relaxometry measurements. A green-laser pulse is first applied to initialize the N-V spins to the  $m_s = 0$  state. After a delay time, t, we measure the occupation probabilities of the  $m_s = -1$ states by applying a rf  $\pi$  voltage pulse at the corresponding ESR frequencies and measure the spin-dependent PL with a green-laser read-out pulse. Note that the rf pulses are delivered with a rf voltage applied across the MTJ. The bottom panel of Fig. 4(e) plots the measured N-V PL as a function of delay time t at three different bias voltages. By fitting the results with an exponential decay function,  $P(t) = A_0 + Ae^{-t/T_1}$  [36,58], where P(t) is the measured photoluminescence, and A and  $A_0$  are constants; the  $T_1$ time of the N-V centers is measured to be 1429, 588, and

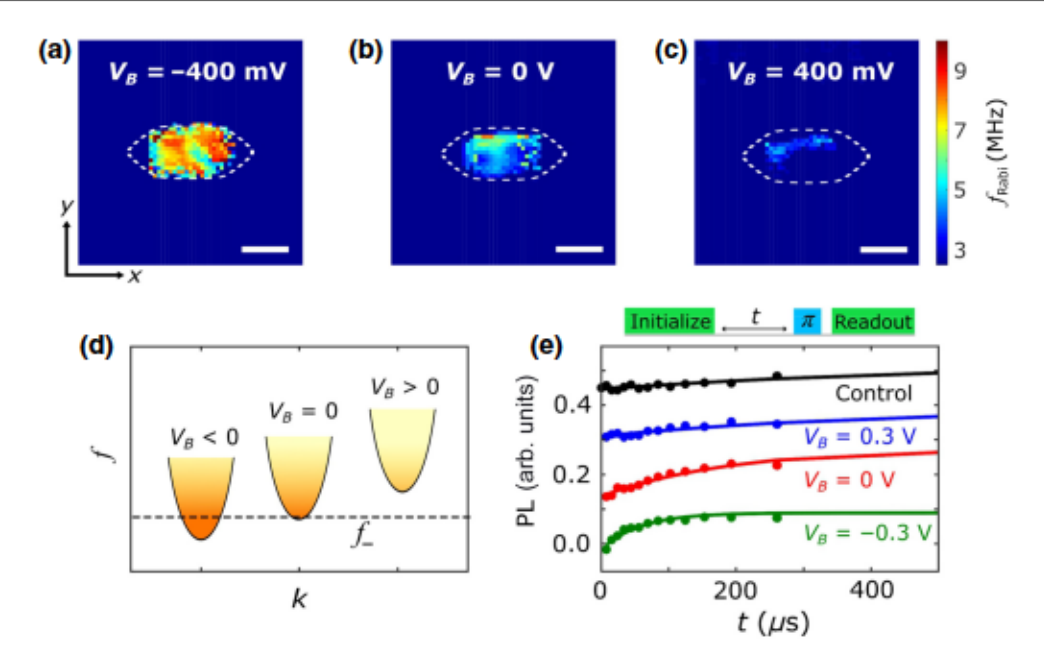


FIG. 4. (a)–(c) 2D maps of Rabi oscillation frequency,  $f_{\text{Rabi}}$ , measured at  $f_-=1.58$  GHz with a bias voltage of -0.4, 0, and +0.4 V, respectively, under an external magnetic field,  $B_{\text{ext}}=460$  G. White dashed line outlines the lateral boundary of the MTJ, and the scale bar is 2  $\mu$ m. (d) Schematic showing the magnon dispersions for various bias voltages and their intersection with the N-V ESR frequency,  $f_-$ . Magnon occupation of the magnetic free layer follows the Bose-Einstein distribution, as indicated by fading color intensities. Positive (negative) bias shifts the magnon band upwards (downwards) relative to  $f_-$ . Dispersions are shifted in k for visual clarity. (e) Top panel, optical and rf voltage pulse sequence used in the N-V relaxometry measurements. Bottom panel, N-V PL intensity measured as a function of delay time t, from which the N-V relaxation time, t0, is extracted to be 1429, 588, and 175 t1 sunder the application of dc bias voltages of 0.3, 0, and t1. V, respectively. Control measurements of N-t1 centers in the diamond microchip give t1 1667 t2.

175  $\mu$ s for bias voltages,  $V_B$ , of +0.3, 0, and -0.3 V, respectively. The electrical tunability of  $T_1$  exploits the voltage-controlled  $f_{\rm FMR}$  of the magnetic free layer, which determines the magnitude of spin noise at the N-V ESR frequency,  $f_-$ , and leads to relaxation of the N-V center spins [36]. Note that  $T_1$  of N-V centers with  $f_-$  tuned slightly above the magnon band ( $V_B > 0$  V) is comparable to the intrinsic relaxation time of N-V centers positioned away from the MTJ ( $T_1$ =1667  $\mu$ s), which is slightly shorter than the value reported in Ref. [37]. In the future, it would also be valuable to characterize the coherence time of N-V centers in the hybrid system.

In summary, we demonstrate coherent control of N-V centers by a resonant MTJ. Exploiting VCMA-driven oscillating stray fields, we achieve local control and electrically tunable control of N-V centers, offering opportunities for developing scalable high-density N-V-based quantum operational units. Due to the large electrical resistance of the insulating tunnel layer of the device, the magnitude of the rf electric current flowing through the MTJ is in the microampere regime, virtually eliminating ohmic losses and the resulting thermal decoherence of nearby N-V centers. We note that the millisecond-long spin-relaxation time  $(T_1)$  remains preserved in N-V centers positioned in nanoscale proximity to the MTJ. These merits highlight the

presented hybrid solid-state system as a promising building block for a broad range of transformative applications in N-V-based quantum computing, sensing, and networking [5,11,16,28,56,57,59,60].

## ACKNOWLEDGMENTS

The authors would like to thank Hanyi Lu for assistance in sample preparation. The authors thank Yaroslav Tserkovnyak, Ilya N. Krivorotov, Pramey Upadhyaya, and Avinash Rustagi for insightful discussions. G.Q.Y., S.L., M.H., and C.R.D. are supported by the U.S. National Science Foundation (NSF) under Grants No. ECCS-2029558 and No. DMR-2046227. N.J.M., H.W., and C.R.D. acknowledge support from the Air Force Office of Scientific Research under Grant No. FA9550-20-1-0319 and its Young Investigator Program under Grant No. FA9550-21-1-0125.

## APPENDIX A: EXTENDED CHARACTERIZATION RESULTS OF MAGNETIC-TUNNEL-JUNCTION DEVICES

The MTJ devices used in this study are prepared by standard photolithography, dry etching, sputtering, and liftoff processes. Details of the nanofabrication have been